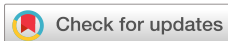


RESEARCH ARTICLE | APRIL 01 2024

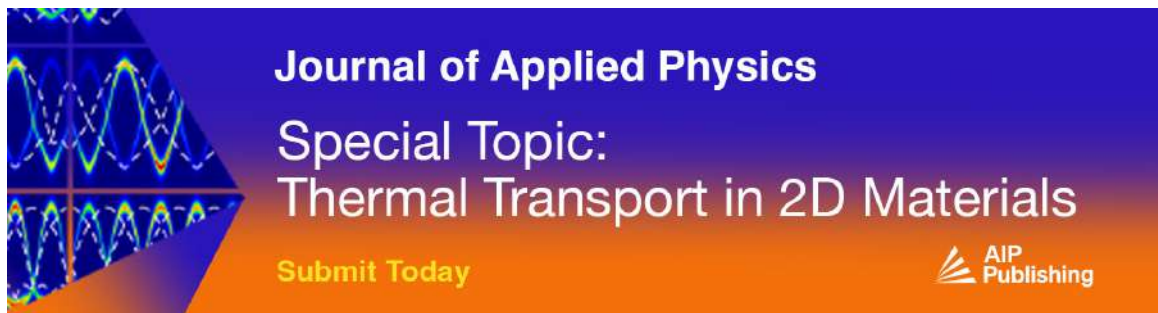
Origin of discrete donor–acceptor pair transitions in 2D Ruddlesden–Popper perovskites F FREE

Setatira Gorji ; Marie Krečmarová ; Alejandro Molina ; Maria C. Asensio ; Andrés F. Gualdrón-Reyes ; Jesús Rodríguez-Romero ; Hamid Pashaei-Adl ; Rodolfo Canet-Albiach ; Luca Schio ; Massimo Tormen; Luca Floreano ; Iván Mora-Seró ; Juan P. Martínez Pastor ; Juan Francisco Sánchez-Royo ; Guillermo Muñoz Matutano  



Appl. Phys. Rev. 11, 021401 (2024)

<https://doi.org/10.1063/5.0176692>



Journal of Applied Physics
Special Topic:
Thermal Transport in 2D Materials

Submit Today



Origin of discrete donor–acceptor pair transitions in 2D Ruddlesden–Popper perovskites

Cite as: Appl. Phys. Rev. **11**, 021401 (2024); doi: [10.1063/5.0176692](https://doi.org/10.1063/5.0176692)

Submitted: 15 September 2023 · Accepted: 12 March 2024 ·

Published Online: 1 April 2024



View Online



Export Citation



CrossMark

Setatira Gorji,¹  Marie Krečmarová,¹  Alejandro Molina,¹  Maria C. Asensio,^{2,3}  Andrés F. Gualdrón-Reyes,^{4,5}  Jesús Rodríguez-Romero,^{4,6}  Hamid Pashaei-Adl,¹  Rodolfo Canet-Albiach,¹  Luca Schio,⁷  Massimo Tormen,⁷  Luca Floreano,⁷  Iván Mora-Seró,⁴  Juan P. Martínez Pastor,^{1,3}  Juan Francisco Sánchez-Royo,^{1,3}  and Guillermo Muñoz Matutano^{1,a)} 

AFFILIATIONS

¹Instituto de Ciencia de Materiales, Universidad de Valencia (ICMUV), 46071 Valencia, Spain

²Instituto de Ciencia de Materiales de Madrid (ICMM), CSIC 28049 Madrid, Spain

³MATINÉE: CSIC Associated Unit (ICMM-ICMUV), Universidad de Valencia, Valencia, Spain

⁴Institute of Advanced Materials (INAM), Universitat Jaume I, Avenida de Vicent Sos Baynat, s/n 12071 Castelló de la Plana, Spain

⁵Facultad de Ciencias, Instituto de Ciencias Químicas, Isla Teja, Universidad Austral de Chile, 5090000 Valdivia, Chile

⁶Facultad de Química, Universidad Nacional Autónoma de México, Circuito Exterior s/n, C.U., Coyoacán, 04510 Mexico City, Mexico

⁷CNR - Istituto Officina dei Materiali (IOM), Laboratorio TASC, 34149 Trieste, Italy

^{a)} Author to whom correspondence should be addressed: guillermo.munoz@uv.es

ABSTRACT

Two-dimensional (2D) van der Waals nanomaterials have attracted considerable attention for potential use in photonic and light–matter applications at the nanoscale. Thanks to their excitonic properties, 2D perovskites are also promising active materials to be included in devices working at room temperature. In this work, we study the presence of very narrow and spatially localized optical transitions in 2D lead halide perovskites by μ -photoluminescence and time-decay measurements. These discrete optical transitions are characterized by sub-millielectronvolt linewidths ($\simeq 120\mu\text{eV}$) and long decay times (5–8 ns). X-ray photoemission and density-functional theory calculations have been employed to investigate the chemical origin of electronic states responsible of these transitions. The association of phenethylammonium with methylammonium cations into 2D Ruddlesden–Popper perovskites, $(\text{PEA})_2(\text{MA})_{n-1}\text{Pb}_n\text{I}_{3n+1}$, particularly in phases with $n \geq 2$, has been identified as a mechanism of donor–acceptor pair (DAP) formation, corresponding to the displacement of lead atoms and their replacement by methylammonium. Ionized DAP recombination is identified as the most likely physical source of the observed discrete optical emission lines. The analysis of the experimental data with a simple model, which evaluates the Coulombic interaction between ionized acceptors and donors, returns a donor in Bohr radius of the order of $\simeq 10$ nm. The analysis of the spectral and electronic characteristics of these single donor–acceptor states in 2D perovskites is of particular importance both from the point of view of fundamental research, as well as to be able to link the emission of these states with new optoelectronic applications that require long-range optically controllable interactions.

Published under an exclusive license by AIP Publishing. <https://doi.org/10.1063/5.0176692>

INTRODUCTION

Research on perovskites (PVKs) has experienced rapid increase and visibility during the last decade due to their use in high performance and low cost solar cells, which represent a potential alternative to the commercially available silicon photovoltaic wafers.¹ Since the discovery of the high light-energy conversion efficiency published in 2009,² the use of perovskite materials has been demonstrated in a large number of photonic devices owing to their interesting properties related to charge transport, excitons and photoexcited carriers generation, bandgap tunability,

and high exciton binding energy in metal halide perovskites (MHPs). This rapid growth in academic activity has merged with another intense field of research, the study of two-dimensional (2D) semiconductors. The isolation of mechanically exfoliated graphene in 2004 has boosted the engineering of an interesting new set of high-quality 2D semiconductor samples that can be prepared very easily. This is the case for 2D lead halide perovskites (LHPs),^{3,4} which have recently been analyzed more closely because of their potential integration in high-efficiency photovoltaics and photonic devices.^{5–8}

As a 2D van der Waals family material, layered perovskites show enhanced stability and structural tunability,^{3,7,9} but with a particular soft lattice and a dynamically disordered structure. Its crystal lattice typically consists of single or multiple organic–inorganic hybrid phases arranged into a Ruddlesden–Popper (RP) structure.¹⁰ The general chemical formula for 2D perovskites is $R_2A_{n-1}B_nX_{3n+1}$, where R_2 is a long organic cation [phenethylammonium (PEA), butylammonium, ethylammonium, etc.], A is a short organic cation [methylammonium (MA), formamidinium (FA), etc.], B is a metal inorganic cation (e.g., lead, tin, and so on), and X is the halide inorganic anion (i.e., chloride, bromide, or iodide).^{7,10–13} In contrast to 3D perovskites, the semiconducting inorganic layer is passivated with insulating organic cations, forming a 2D natural quantum well (QW) structure. The thickness of this natural QW is controlled by the n value,⁹ which labels the number of inorganic monolayers building the QW structure (from $n = 1, 2, 3$ to $\sim \infty$).^{7,9} As a consequence, the n value defines the electronic and optical properties, as the bandgap energy increases as the n value decreases. The 2D RP perovskites show a strong quantum confinement and a weak dielectric screening, leading to excitonic states with binding energies up to several hundreds of millielectronvolt for $n = 1$ (strictly 2D structure),³ which leads to good exciton stability up to room temperature¹⁴ and following the emergence of large fine structure energy shifts.^{15,16}

The intense excitonic features present in small n value 2D MHPs play an important role in the development of optoelectronic devices. First, and as a negative consequence, the high excitonic binding energy characteristics of small n values 2D MHPs reduce the overall photocurrent generation for solar cell applications.¹⁷ Thus, for overcoming such drawback, larger n values (namely, 2D–3D structures) with smaller excitonic binding energies can be used.¹³ As a consequence, low- n phases that exhibit enhanced excitonic effects are more commonly used for optical emission devices, or light–matter interaction platforms as excitonic polariton lasers and condensates,^{18,19} for example. However, there are alternative approaches to produce different optoelectronic applications using these highly excitonic 2D perovskites. It has been reported that molecular doping by a small and highly electron acceptor complexes of 3,4,5,6-tetrachloro-1,2-benzoquinone (TCBQ) into $n = 1$ LHPs containing naphthalene cations serving as a donor, give rise to the formation of donor–acceptor pairs (DAPs) within the organic layer.²⁰ These DAP organic species located between the inorganic layers have been used to increase the electrostatic screening of the exciton, and hence to tune the excitonic binding energy in 2D hybrid layered perovskites.^{13,20} However, this charge transfer has not been observed when using bulkier phenethylammonium (PEA) organic cations as the only layer spacers, which isolate the inorganic sheet and thus inhibit the charge transfer processes at the inorganic crystal interface. The same consequence is found when using MHPs with $n > 1$ that reduces the excitonic character.¹³ The optical signatures of donor and acceptors as shallow defects in single-crystal hybrid LHPs have been also studied.^{21,22} Particularly, discrete DAP optical features have been reported in bulky $CH_3NH_3PbI_3$ single crystals, which were associated with the presence of native shallow defects.²³ In this single-crystal LHP, μ -photoluminescence (μ -PL) experiments revealed both structureless and well-structured emission features below the free exciton energy. In samples positions with high defect density, DAP emission is observed as a broad emission band with particular power, temperature, and dynamical dependencies.

However, at low defect density sample positions, the DAP emission is characterized by sharp single transitions, with full width half maximum (FWHM) on the order of 3 meV. The ensemble parametric dependence of the DAP optical spectra with excitation power, temperature, or time dynamics represents a well-known behavior, which is manifested by the statistical evolution or large collection of DAP transitions. This study with high spatial resolution techniques gave the opportunity to analyze single DAP (S-DAP) optical transitions, as already carried out with other materials, like 2D hexagonal boron nitride (hBN).²⁴ As a consequence, there is an active and open debate about the identification of extrinsic optical transitions in the emission spectra of LHPs,²⁵ where the analysis and the understanding of the properties of single DAP states can be revealed as an important tool with the correct combination with other spectral techniques.

In this work, we measured and identified discrete DAP spectral lines at low temperatures, as long-lived optical transitions in 2D RP-based materials. By means of spatial and time-resolved μ -photoluminescence (μ -PL), we recorded optical transitions with narrow linewidths, as low as $\simeq 120 \mu\text{eV}$ FWHM, and time decays as long as 8.6 ns. Excitation power and temperature-dependent spectral measurements are compatible with the presence of DAP transitions. X-ray photoelectron spectroscopy (XPS) has been employed to identify chemical processes giving rise to electronic states responsible to DAP-related optical transitions. In particular, the DAP appears to be related to the exchange of methylammonium (MA) molecule and Pb atoms present in 2D LHPs samples with phase thickness $n = 2$ (for $n = 1$, only PEA is present forming the strictly 2D LHP), leading to optical recombination in a broad spectral range between two excitonic transitions. This claim is supported with complementary optical spectroscopic data by means of μ -Raman spectra. Our experimental effort is accompanied by predictions from a simple model to calculate the density of states (DOS) as a function of DAP binding energy, which is built up by the attractive Coulombic interaction between their net charges. Using this analysis, we extract a rough estimation of the effective donor/acceptor in Bohr radius ($\simeq 10 \text{ nm}$), one order of magnitude larger than the excitonic Bohr radius. Our complete dataset and analysis help to understand the principal signatures and elucidate the nature of the DAP state in microexfoliated 2D RP LHPs, and its relationship with the selected cation spacer. The ability to isolate single DAP state can potentially be used to study advanced light–matter strategies with very sharp and bright optical transitions with potential high non-linearity, as related to the DAP binding energy and Bohr radius tunability. These findings could stimulate the analysis of important drawbacks for the use of 2D LHP semiconductors for the development of light photodetectors and light-emitting devices, or to produce new alternative routes to the study of fundamental light–matter interaction effects.^{26–29}

RESULTS

Synthesis and preparation

Two different phases of 2D RP LHP single crystals with the lowest quantum well thicknesses corresponding to $n = 1$ and $n = 2$ were synthesized (see Materials and Methods for more details). The crystal lattice consists of an inorganic octahedral layer that is sandwiched by long organic cations, forming 2D quantum well structures. Figures 1(a)–1(c) show the crystal structures of both PEA_2PbI_4 ($n = 1$) and $PEA_2MAPb_2I_7$ ($n = 2$) phases. They are made up of a single layer ($n = 1$) and a double layer ($n = 2$) of perovskite inorganic octahedral

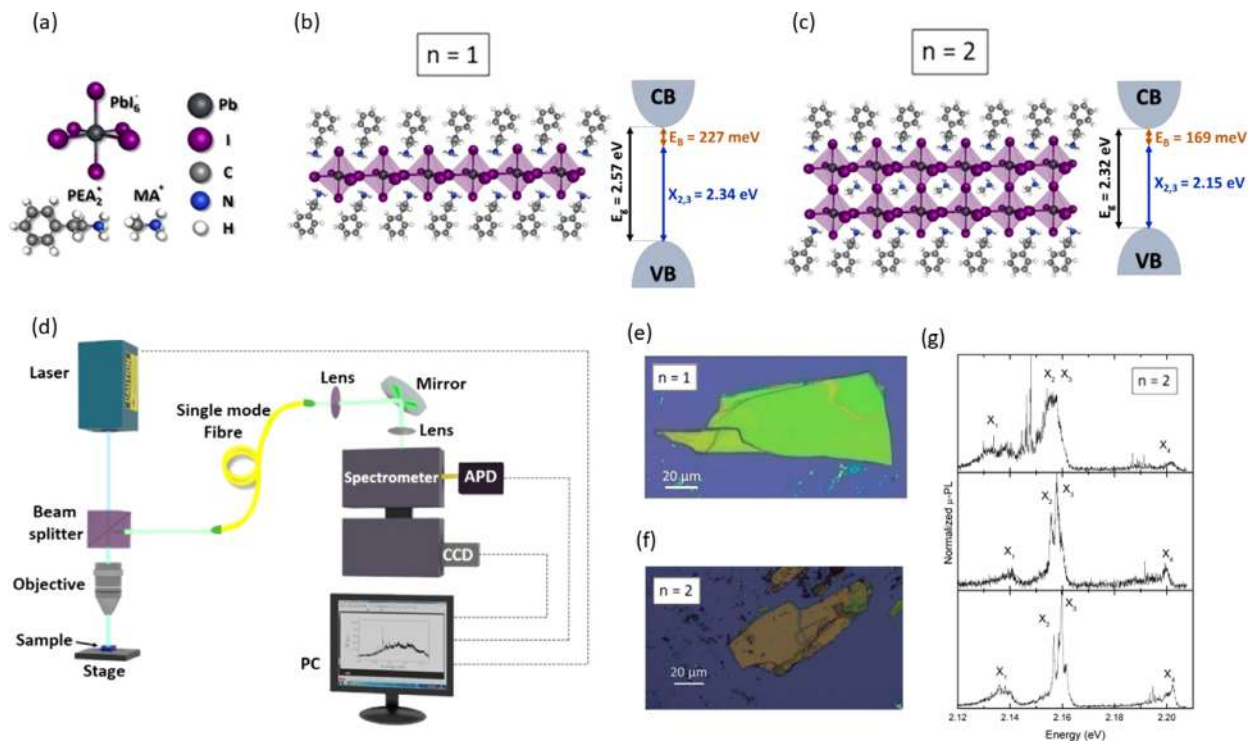


FIG. 1. (a) 2D perovskites are composed of inorganic octahedral $(\text{PbI}_6)^-$, short organic methylammonium $(\text{MA})^+$ cation, and long organic Phenethylammonium $(\text{PEA}_2)^+$ cation. (b) Crystal structure of a monolayer of 2D perovskite PEA_2PbI_4 crystal with a quantum well thickness of phase $n = 1$, where a single octahedral sheet is sandwiched by a PEA_2 organic spacer. The level structure indicates its energy levels diagram, with valence band (VB), conduction band (CB), electronic bandgap (E_g), the free exciton optical transition ($X_{2,3}$), and the exciton binding energy (E_b), including their values obtained from Ref. 30. (c) Crystal structure of a monolayer of 2D perovskite $\text{PEA}_2\text{MAPb}_2\text{I}_7$ crystal with a quantum well thickness of phase $n = 2$, consisting of two octahedral sheets intercalated with short MA molecules, sandwiched by a PEA_2 organic spacer. The level structure indicates its energy levels diagram as before, but for the phase $n = 2$. (d) Scheme of the confocal μ -photoluminescence spectroscopy system with a steady state and time-resolved detection. A blue excitation laser beam with wavelength of 450 nm is focused through a beam splitter and an objective with $\text{NA} = 0.42$ to the focal plane of 2D perovskite flake is used to achieve micro-localization. Steady-state μ -photoluminescence is detected by a charge-coupled device (CCD) camera and time-resolved μ -PL by the avalanche photodiode (APD). Molecularly thin exfoliated flake of 2D perovskites with phase $n = 1$ (e) and $n = 2$ (f) with tens of μm lateral size. (g) Examples of the μ -PL spectrum containing four excitonic transitions, labeled as X_1 , X_2 , X_3 , and X_4 , for a $n = 2$ sample.

flakes composed of $(\text{PbI}_6)^-$ anions sandwiched by long organic $(\text{PEA}_2)^+$ cations, which serve as spacers. The inorganic double layer is intercalated by short organic $(\text{MA})^+$ cations for $n = 2$. Only the $n = 1$ phase has a well-defined structure, whereas small inclusions of another n phase are formed for a higher inorganic flake thickness $n > 1$.³¹

We used a confocal microscope to measure μ -PL and time-resolved μ -PL (μ -TRPL), as shown in Fig. 1(d). In our setup, the samples are held in the cold finger of a closed-cycle He cryostat (see Materials and Methods for more details) to investigate the optical characteristics of a large number of exfoliated flakes of 2D perovskites single-crystal PEA_2PbI_4 ($n = 1$) and $\text{PEA}_2\text{MAPb}_2\text{I}_7$ ($n = 2$) at 4 K, with spectral system resolution of 100 μeV at 532 nm and sub-diffraction limited spatial resolution (≈ 500 nm). Synthesized crystals can be easily exfoliated down to a single monolayer, thanks to the relatively weak van der Waals interlayer coupling. In this study, synthesized single crystals of both phases were exfoliated onto SiO_2/Si substrates using scotch tape (see Materials and Methods for more details). Exfoliated single-crystal flakes with a typical lateral size of tens to hundreds of micrometers and a thickness of tens of nanometers are shown in Fig. 1(e) ($n = 1$) and Fig. 1(f) ($n = 2$). Exfoliation reduces the

occurrence of unwanted hybrid phase formation³¹ and leads to a strictly flat crystal orientation to the substrate.³²

μ -photoluminescence and time decays

The identification of the nature of the excitonic states observed in the 2D LHPs is still under debate in the academic community. In previous studies, four different discrete excitonic transitions contributing to PL and absorption spectra in 2D LHP single crystals have been measured and calculated when including spin-orbit interaction.^{15,16} Accordingly, Fig. 1(g) shows three examples of the μ -PL spectrum containing four excitonic transitions labeled as X_1 , X_2 , X_3 , and X_4 , for $n = 2$ sample. As it is shown, the emission from X_1 and X_4 transitions is very weak compared to the central emission with contributions of X_2 and X_3 . Here, we focus our attention to the analysis of the spectral characteristics for the first three excitonic transitions (X_1 , X_2 , and X_3), for both $n = 1$ and $n = 2$ samples. The intensity of the fourth peak, X_4 , whose optical transition appears at higher energy, is weak and not always measurable. We could not provide clear identification or excitonic assignment of this fourth transition, which could be tentatively explained by mixed dark-bright states³³ or spin-orbit coupling.^{15,16}

In this sense, the origin and dynamics of this higher energy optical transition are out of the scope of our analysis.

Figure 2(a) displays a typical optical spectrum for the $n = 1$ phase samples covering our spectral range of interest. We tentatively identify the two central peaks X_2 and X_3 (in the following will be labeled as $X_{2,3}$, due to its proximity in energy) to free exciton recombination [see Fig. 1(f)].^{25,34} However, the exciton may recombine through other

paths, such as intrinsic optical transitions (e.g., self-trapped excitons, biexcitons, triexcitons, or phonon replicas) or extrinsic optical transitions, as excitons bound to defects.³ The general and basic excitonic trends will be summarized in the following. Figure 2(b) shows the data dispersion of FWHM, as extracted from fitting the experimental spectra to two Lorentzian profiles for both X_1 and $X_{2,3}$ exciton transitions. In the case of the main excitonic transition at ~ 2.344 eV $X_{2,3}$

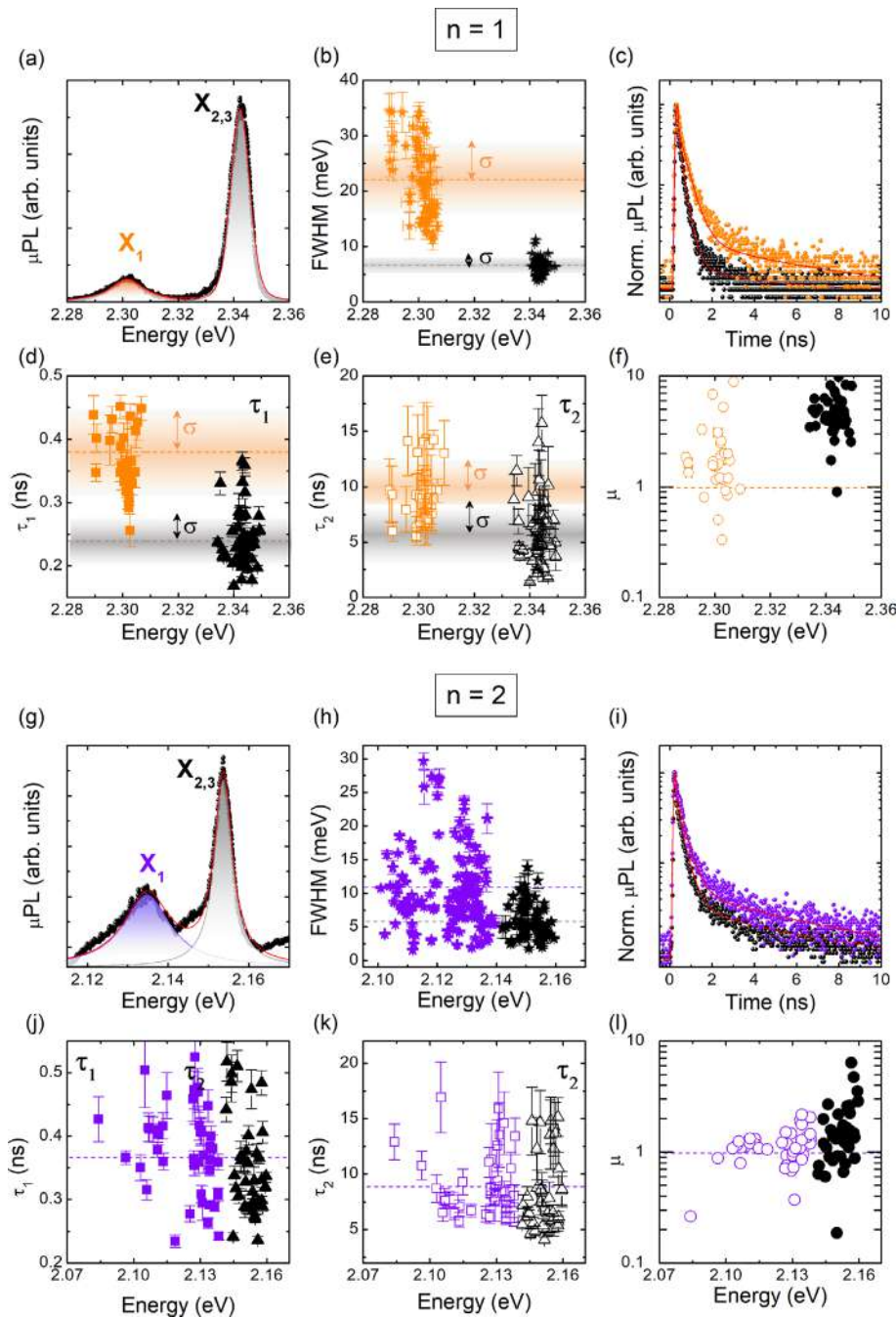


FIG. 2. μ -Photoluminescence (μ -PL) and time-resolved μ -photoluminescence (μ -TRPL) general characteristics at low temperature (4 K). An example of measured μ -PL spectra for phase (a) $n = 1$ and (g) $n = 2$. $X_{2,3}$ and X_1 optical transitions correspond to the three main excitonic transitions. Statistics of X_1 and $X_{2,3}$ peak line-width full width at half maximum (FWHM) as a function of emission energy of X_1 and $X_{2,3}$ for phase (b) $n = 1$ and (h) $n = 2$. Example of TRPL of X_1 and $X_{2,3}$ on a 10 ns timescale for phase (c) $n = 1$ and (i) $n = 2$. Statistics of X_1 and $X_{2,3}$, fast decay (τ_1) for phases (d) $n = 1$ and (j) $n = 2$, and long decay (τ_2) for phases (e) $n = 1$ and (k) $n = 2$. Statistics of the relative intensity (μ) between both fast and slow radiative channels of X_1 and $X_{2,3}$, as a function of emission energy for phases (f) $n = 1$ and (l) $n = 2$.

(Black star), we deduce a mean FWHM = 6.5 meV with a standard deviation $\sigma = 1.48$ meV. For the X_1 transition (Orange star) at 2.290–2.305 eV, the data return larger mean FWHM = 22.1 meV and $\sigma = 6.8$ meV. When analyzing X_1 and $X_{2,3}$ recombination in samples with $n = 1$, both transitions are clearly differentiated by their spectral signatures. Figure 2(c) shows an example of two μ -TRPL spectra for both X_1 and $X_{2,3}$ transitions present in the $n = 1$ phase, which are characterized by two decay channels (fast and slow decay times, τ_1 and τ_2 , respectively). The best fits for these transients [continuous red lines in Fig. 2(c)] yield fast decay times of 0.241 ± 0.006 ns and 0.393 ± 0.019 ns for X_1 and $X_{2,3}$ transitions, respectively.

Figures 2(d) and 2(e) show the statistical sampling of the decay time measurement for both fast and slow components. The mean value of $X_{2,3}$ is $\tau_1 = 0.24$ ns, with $\sigma = 0.04$ ns, while for X_1 $\tau_1 = 0.38$ ns, with $\sigma = 0.07$ ns. Additionally, the residual long τ_2 shows mean value of 6 ns for $X_{2,3}$ transition with $\sigma = 2.8$ ns, while for X_1 , it reaches a mean value of 9.5 ns, with $\sigma = 2.7$ ns [Fig. 2(e)]. This residual long component found in the decay trace can be associated with the conventional avalanche photodiode (APD) time response function, which is clearly several decades lower in magnitude³⁵ or a second long decay associated with real optical recombination processes, as observed in perovskites mostly at room temperature.^{36,37} In order to provide quantitative information about the strength between these two fast and slow dynamics, we analyzed the relative intensity between both components. To do this, we define new parameter (μ) to compare the weight of the coincidences counts from both decay channels. Hence, we define it as $\mu = \frac{I_F(T)}{I_S(T)}$, where $I_{F/S}(T) = \int_{t=0}^{t=T} a_1 \exp^{-t/\tau_1} \cdot dt$, and T is the laser period. In this sense, the μ value will describe situations where the fast decay dominates ($\mu > 1$), both channels have similar contribution ($\mu \sim 1$), or the slow decay dominates ($\mu < 1$). As shown in the plot of Fig. 2(f), $\mu > 1$ for almost all cases, both for X_1 (open orange circles) and $X_{2,3}$ (filled black circles). Accordingly, the fast decay time (≈ 240 ps) always dominates over the long decay time in samples with the RP phase $n = 1$, and hence, the long decay is identified as the APD detection tail. We now present a similar analysis carried out in samples prepared with the RP phase $n = 2$. Figure 2(g) shows an example of the μ -PL spectra of a representative sample. First, and as before, we focus our attention to the first three excitonic transitions. Following similar arguments as described earlier, these are labeled as X_1 , $X_{2,3}$ transitions. The increase in n in the 2D RP perovskite produces a clear red shift of its optical emission energy [see Fig. 1(f)]. The $X_{2,3}$ transition is observed now at ~ 2.15 eV, hence shifted almost 200 meV toward lower energies concerning its $n = 1$ counterpart. Figure 2(h) shows the dispersion of the FWHM values deduced from X_1 (Violet star) and $X_{2,3}$ (Black star) μ -PL lines vs the emission peak energy, where the $X_{2,3}/X_1$ mean FWHM is 5.7/10.4 meV, with $\sigma = 2.5/5.8$ meV. Here, we clearly identify larger linewidth dispersion than in the previous statistical analysis made in the RP $n = 1$. We tentatively associate this effect to the more complex electronic scenario present in the $n = 2$ phase.

Similarly, it occurs with time decays. Figure 2(i) shows one example of the X_1 and $X_{2,3}$ μ -TRPL measurements, displaying the same double component of for both X_1 and $X_{2,3}$ peaks as in the $n = 1$ phase. Figures 2(j) and 2(k) show the statistics of the fast (τ_1) and slow (τ_2) decay times for both X_1 and $X_{2,3}$ transitions. The mean τ_1 value of $X_{2,3}$ is 0.35 ns, with a $\sigma = 0.07$ ns, while for X_1 is 0.38 ns, with a $\sigma = 0.07$ ns. The mean τ_2 value of $X_{2,3}$ is 8.4 ns, with a $\sigma = 3.5$ ns, while for X_1 is 8.8 ns, with a $\sigma = 2.8$ ns. The principal difference between $n = 1$ and

$n = 2$ μ -TRPL is the higher observed dispersion for the $n = 2$ phase, although here mean values are slightly larger than previously. This larger dispersion reinforces the claim that a more complex scenario is present in this thicker phase. Finally, and as before, we analyzed the relative intensity of both short and long decay channels with the parameter μ . Figure 2(l) shows the dispersion of μ for the phase $n = 2$. As is shown, almost all values are situated close to $\mu \sim 1$ or $\mu > 1$. This means that the fast decay still dominates in both $X_{2,3}$ (filled black circles) and X_1 (open violet circles) measurements, and thus, the long decay can be associated in most cases with the APD detector tail, as before. However, in a small fraction of cases, we appreciate a dominating contribution of the slow component ($\mu < 1$).

Donor-acceptor pair optical emission

The higher complexity observed in recombination dynamics in the RP $n = 2$ phase is accompanied in some cases with the presence of narrow optical transitions, whose central peak energy position ranges between X_1 and $X_{2,3}$ excitonic optical transitions [see Figs. 3(a), 3(c), and 3(e)]. In our analysis, this third kind of peaks has been found in different points across the surface of different flakes with a frequency $\approx 11\%$; hence, a non-negligible probability of finding such discrete emission lines labeled here as DAP states, attending to their origin, as elucidated below. Figures 3(a), 3(c), and 3(e) (top panel) show μ -PL spectra of $n = 2$ phase samples where the discrete DAP transitions are present. We performed multi-Lorentzian fitting in all recorded spectra to extract more accurately the spectral parameters of the DAP transitions. The contribution of X_1 and $X_{2,3}$ optical emission lines is depicted with violet and black shadows, whereas the blue shadows indicate the emission from DAP transitions, with characteristic FWHMs ranging from 150 μ eV up to ≈ 5 meV. The amplitude of the transition is more than 20 times the Poissonian RMS noise of the baseline; which is more important, the optical transition reaches a steady state, i.e., the DAP optical transition can be continuously monitored in time, maintaining its amplitude and intensity. In this sense, it is completely discarded any spurious signal as its source, like cosmic rays.

As before, we performed μ -TRPL spectra for X_1 , $X_{2,3}$, and DAP transitions, as shown in Figs. 3(b), 3(d), and 3(f) (black, violet, and blue, respectively). Here, X_1 and $X_{2,3}$ transitions show similar behavior than before: fast decay dominating over the slow decay. However, the sharp DAP transition presents in the RP $n = 2$ phase shows a DAP dynamics (blue scattered dots) characterized by a fast decay followed by a slow decay being now the dominant intensity contribution.

The dependence of the integrated μ -PL intensity on the excitation power for X_1 and $X_{2,3}$ excitonic transitions (filled squares and triangles) and the DAP transitions (filled circles) is shown in a log-log plot in Fig. 3(g). The slope of $X_1/X_{2,3}$ is 0.78/0.81, whereas the DAP transition exhibits a very small slope (0.32) and even saturates. This weak dependence on the power excitation is clearly related to a finite number of DAP states, which are being filled with photogenerated carriers after a relatively low incident laser power; hence, it is a first signature about their origin as donor-acceptor pair recombination.^{38,39} The most accepted experimental proof of DAP recombination is the blue shift of the peak energy as a function of excitation power. However, this characteristic blue shift is commonly explained as a consequence of the dynamical filling of DAP density of states for different energies (different states due to different DAP distances) and hence as an ensemble manifestation of the DAP nature. In our work, we are

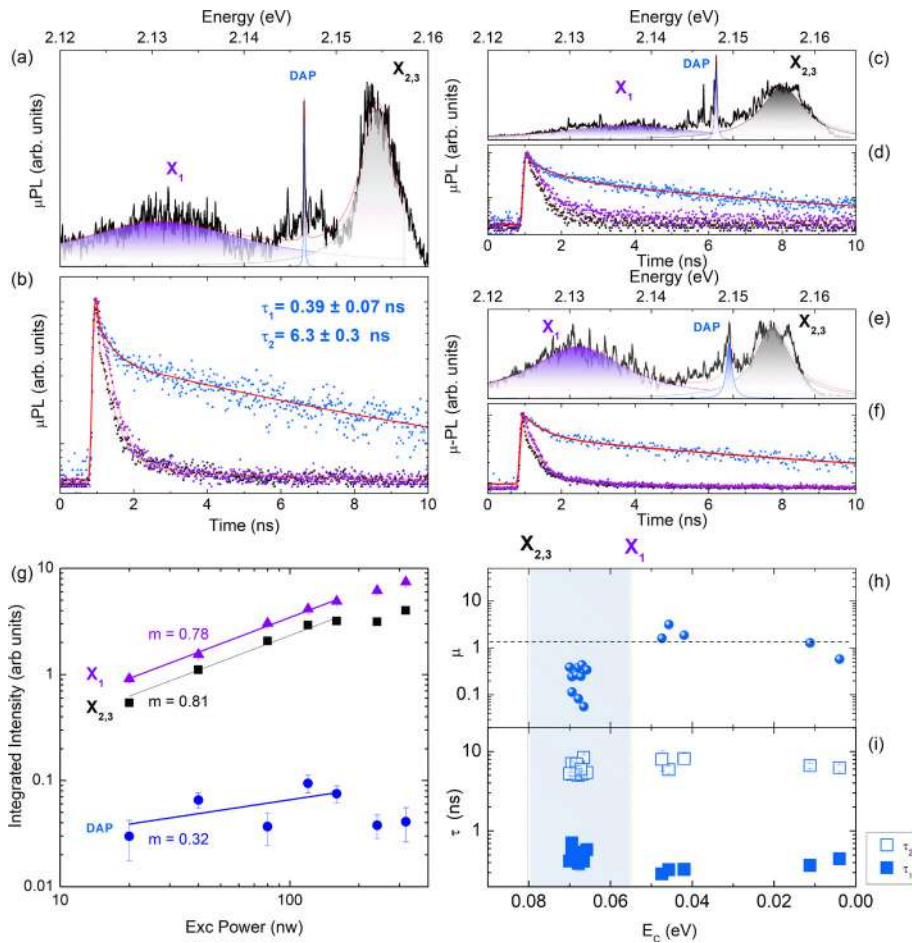


FIG. 3. Donor–acceptor pair (DAP) optical emission signatures in $n = 2$ samples. (a), (c), and (e) μ -Photoluminescence spectra of three different samples with highlighted X_1 (violet color), $X_{2,3}$ (black color), and ionized donor–acceptor pair emission peaks (DAP, blue color) with their corresponding μ -time-resolved photoluminescence traces (b), (d), and (f) of the observed $X_{2,3}$ (black scattered dots), X_1 (violet scattered dots), and DAP (blue scattered dots) optical transitions. (g) Integrated intensity as a function of the excitation power in a log–log plot for X_1 , $X_{2,3}$ and DAP optical transitions present in $n = 2$ example sample, where DAP transition shows clear sublinear slope (m). (h) statistics of the relative intensity parameter (μ) as a function of the DAP binding energy (E_C). (i) Statistics of fast (τ_1) and slow (τ_2) decay times as a function of the DAP binding energy (E_C).

measuring structured DAP transitions, consisting of discrete emission lines associated with sufficiently separated DAP energy states, due to very low DAP defect density within the incident excitation spot.

Figure 3(h) shows the evolution of μ parameter as a function of the DAP binding energy (E_C). The calculation of E_C will be described in the Discussion section. As can be seen, there is a clear energy range where the radiated intensity from the slow decay channel dominates over the fast decay ($\mu < 1$), where this fast decay contribution is almost negligible; this energy range is marked with a bluish shadow in Figs. 3(h) and 3(i). The residual presence of the fast decay when filtering the DAP transition can be associated with the background emission from X_1 and $X_{2,3}$ transitions. Figures 3(a), 3(c), and 3(e) show how the Lorentzian tail of X_1 and $X_{2,3}$ produces an overlap with the DAP peak energy position, and hence, it is plausible that μ -TRPL traces can contain a minor contribution from X_1 and $X_{2,3}$ excitonic recombination lines.

Figure 3(i) shows the statistical sampling of DAP τ_1 and τ_2 time decays as a function of E_C . We can assume that DAP optical transitions are characterized by longer time dynamics, which is in correspondence with its sharpest spectral features. However, neither decay nor FWHM are Fourier transform-related, and hence, we should expect the effect of extra carrier dynamics mechanism in the DAP recombination, even

though our limited spectral resolution ($\approx 100 \mu\text{eV}$) does not completely excludes the reduction of our capacity to estimate the real FWHM values. To obtain the full description of the characteristics and magnitude of the correlation time and dephasing process acting on the DAP transition, it will be necessary to perform alternative interferometric measurements.⁴⁰

A second distinctive characteristics of the optical emission of DAPs is the strong blue shift of its emission peak energy as a function of temperature.^{22,41} The DAP band is usually associated with a large distribution of pairs. Each pair is defined by the relative distance R between the donor and acceptor, and therefore different binding energies. As soon as the thermal energy provided to the DAP distribution is high enough to equal the binding energy, the donor–acceptor pair will dissociate/quenche. The critical temperature to produce this dissociation will be smaller for pairs with lower binding energies. As a consequence, the collective or ensemble DAP PL will show an effective blue shift as the temperature increases, associated with the selective quenching of the less bonded DAPs. However, optical transition from single DAP will not follow this last collective blue shift evolution. As the transition is produced by the recombination from a single pair, its peak energy temperature evolution will follow the bandgap energy shift.

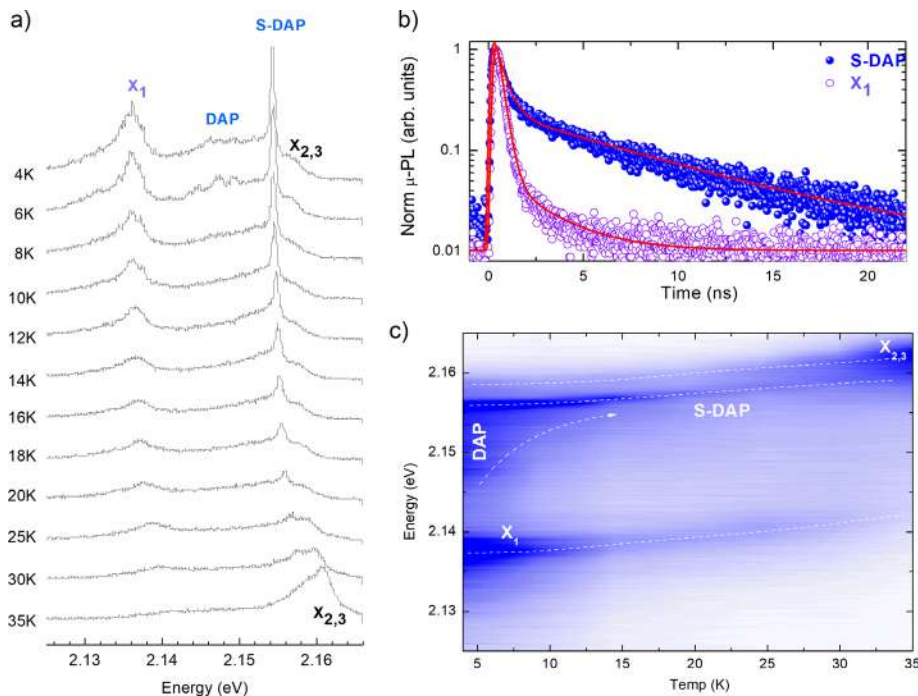


FIG. 4. Evolution with temperature of the μ -photoluminescence of a flake of phase $n=2$. (a) Measurement of the μ -photoluminescence spectra between 4 and 35 K. Four main emission bands are identified, two of them associated with excitonic emission (X_1 and $X_{2,3}$) and two others associated with Donor–Acceptor optical emission (DAP and S-DAP). (b) Time-resolved photoluminescence traces of the observed X_1 (open dots) and S-DAP (filled dots) transitions. (c) Contour plot representation of the data plotted in panel (a). Here, dotted lines are guides for the eye.

In Fig. 4, it is represented the identification and the evolution with temperature of the spectral lines present in a $n=2$ exfoliated flake. In Fig. 4(a), four distinct optical transitions are labeled and analyzed as a function of sample temperature. Two of them corresponding to excitonic transitions (X_1 and $X_{2,3}$) and two others associated with the emission of donor–acceptor optical transitions: DAP for the case of the ensemble donor–acceptor and S-DAP to indicate the optical emission of a single donor–acceptor pair (defined by a narrow PL line).

Figure 4(b) shows the μ -TRPL transients of the X_1 and S-DAP-labeled transitions. As it is shown, the X_1 transient is mainly composed of a fast and single decay with a very weak second slow decay, while in the case of S-DAP, the transient shows two clear components, corresponding with the fast and slow decays discussed before. The main contribution from X_1 transition comes from the fast decay ($\mu=5.7$), while the S-DAP optical emission is dominated by the slow decay ($\mu=0.43$). We identify the sharp and narrow spectral transition together with the slow decay dominance with the recombination of a single DAP (S-DAP).

Figure 4(a) shows the temperature evolution of the four transitions. As the sample temperature increases, the band identified as DAP (ensemble) very soon begins to undergo quenching of the emission at its low energy side, producing an abrupt effective blue shift. Such a large-effective blue shift, it is commonly identified in the literature as the fingerprint of the DAP transition.^{22,41} In the contour plot shown in Fig. 4(c), this effective blue shift is indicated by a curved dotted arrow, showing that less bonded pairs with optical emission located at lower energies are quenched at very low temperatures (5–15 K). The peak energy of the S-DAP transition associated with the emission of a single donor–acceptor pair would evolve with temperature following the energy gap, like the free exciton transitions. However, its optical

intensity is suffering a large intensity reduction above ≈ 12 K. At a temperature around 25 K, the optical emission from S-DAP is residual, and the $X_{2,3}$ excitonic optical contribution starts to dominate. Here, we can report two important consequences: first, since S-DAP optical intensity practically vanishes at a temperature above 30 K, we can associate its thermal quenching mechanism with a relatively small activation energy, again compatible with a DAP transition; and second, when the DAP is thermally dissociated, the excitonic contribution $X_{2,3}$ is dominant. This behavior has been found previously in the literature and explained as a promotion from DAP states to bound exciton complexes.²²

The set of measurements of the optical emission as a function of excitation power, temperature, and time provides a broad experimental basis for assessing the association of these narrow optical transitions found in the $n=2$ phase as coming from the recombination of donor–acceptor pairs. However, in order to extend the evaluation of this hypothesis, we have analyzed the photoemission properties of the different phases of 2D perovskite samples.

XPS experiments have been performed to identify the electronic states that originate the DAP transition. Figures 5(a)–5(c) show the Pb 4f, I 3d, and N 1s core-level spectra acquired in both phases $n=1$, $n=2$ and in a reference bulk sample. These measurements are expected to provide direct information about the oxidation degree and chemical environment of each atomic species. In the bulk samples, Pb 4f and I 3d core-level spectra are dominated by Pb^{+2} and I^{-1} spin-orbit doublets with a $Pb4f_{7/2}$ component located at 138.1 eV and a $I3d_{5/2}$ component at 618.7 eV, respectively [Figs. 5(a) and 5(b)]. These components are attributable to Pb and I atoms in the inorganic octahedral anions. Together with the main Pb^{+2} core-level signal, we have observed traces from Pb^0 (with its $Pb4f_{7/2}$ component located at 135.9 eV), which reveals the presence of metallic Pb segregated to the

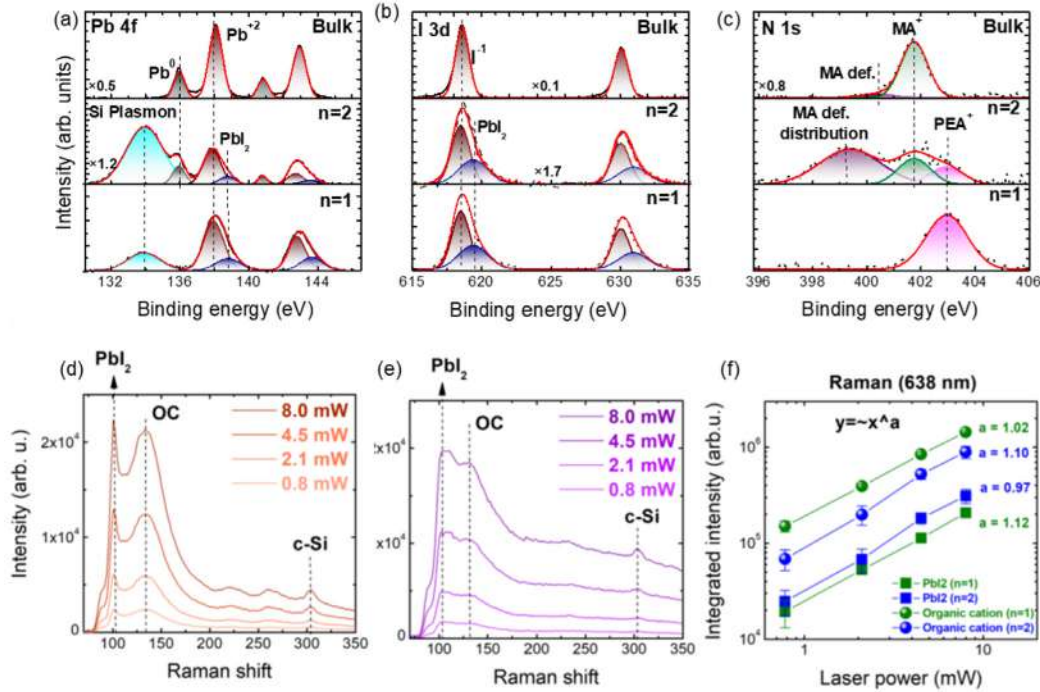


FIG. 5. XPS spectra of (a) Pb 4f, (b) I 3d, and (c) N 1s core levels measured in $n = 1$, $n = 2$, and bulk lead iodine perovskite crystal phases. The broad peak appearing on the low binding energy side of Pb 4f spectra for $n = 1$ and 2 samples (shaded in light blue), corresponds to the second replica of the Si 2p plasmon (plasmon energy of ~ 17.8 eV from Si 2p_{3/2}). (d) and (e) Raman spectra of phase (d) $n = 1$ and (e) $n = 2$ 2D HPs as a function of laser power with marked peaks attributed to PbI_2 organic cation (OC) and c-Si vibration modes. (f) Raman integrated intensity of the PbI_2 and organic cation-related peaks as a function of the laser power for both phases showing a linear dependency as a function of laser power.

surface of our test bulk sample [upper panel in Fig. 5(a)]. As in bulk samples, traces from Pb^{+2} and Pb^0 species have been observed in the Pb 4f and I 3d core-level spectra acquired in $n = 2$ samples. However, we have detected additional Pb 4f and I 3d doublets, these appearing at the high energy side of the main Pb^{+2} and I^{-1} doublets with their $Pb4f_{7/2}$ and $I3d_{5/2}$ components located at 138.9 and 619.5 eV [middle panels in Figs. 5(a) and 5(b)], respectively. These results, together with the fact that these new Pb 4f and I 3d components exhibit an atomic Pb/I ratio of $\sim 0.3 \pm 0.1$, suggest that their origin may be related to the presence of PbI_2 -like species at the sample surface. In the Pb 4f and I 3d core levels measured in the $n = 1$ sample [lower panels in Figs. 5(a) and 5(b)], spectra reveal the presence of Pb and I atoms in PbI_2 -like species coexisting with the Pb^{+2} located in the lead-iodide inorganic octahedral configuration. However, no traces from metallic Pb^0 have been observed, interestingly.

μ -Raman spectroscopy results shown in Figs. 5(d)–5(f) also support previous oxidation assignment. We identify two intense peaks centered at 102 and at 132 cm^{-1} for both $n = 1$ [Fig. 5(d)] and $n = 2$ [Fig. 5(e)] phases. The lower-frequency peak is associated with the PbI_2 and the higher-frequency peak to organic cation molecule vibrations.^{1,2} Another less intense peaks centered at 224 and 261 cm^{-1} could be attributed to organic cation vibrations⁴² and a peak located at 303 cm^{-1} to c-Si vibrations from the Si/SiO₂ underlying substrate. By a closer examination of the Raman spectra can be found that the intense peak related to the vibration of the organic cation is relatively broad

with $FWHM = 40$ cm^{-1} for both phases $n = 1, 2$. On the other hand, the lowest frequency intense peak attributed to vibration of the PbI_2 shows more differences between $n = 1, 2$ phases. The PbI_2 -related peak is sharper for $n = 1$ ($FWHM = 8$ cm^{-1}) than for $n = 2$ ($FWHM = 15$ cm^{-1}), suggesting a noticeable better crystal quality of $n = 1$ phase. This conclusion supports our previous evidence for a more complex carrier dynamics scenario when studying the $n = 2$ phase. Figure 5(f) shows the integrated intensity as a function of excitation power of the Raman spectra of PbI_2 and the organic cation peaks, for both $n = 1, 2$ phases. As it is shown, the evolution follows a linear power dependency (the slope is $\simeq 1$, for all samples).

The photoemission and Raman results indicate a different chemical behavior and crystal quality as going from one kind of sample to the other, which imply a rich structural-dependent chemical activity. Of course, Pb 4f and I 3d spectra appear dominated by signals coming from (pristine) inorganic octahedral sheets in all kinds of samples [Figs. 5(a) and 5(b)]. However, we have detected metallic Pb^0 , but not PbI_2 -like species, in the bulk sample [upper panels in Figs. 5(a) and 5(b)] and we have detected PbI_2 -like species, but not metallic Pb^0 , in the $n = 1$ samples [lower panels in Figs. 5(a) and 5(b)]. Only in the $n = 2$ samples, both metallic Pb^0 and PbI_2 -like species coexist [middle panels in Figs. 5(a) and 5(b)]. Structurally, $n = 1$ and bulk samples differ one from each other, precisely, in the nature of their organic components: MA^+ cations constitute the organic species in bulk samples, whereas PEA_2 ones are those of the $n = 1$ ones. These facts suggest

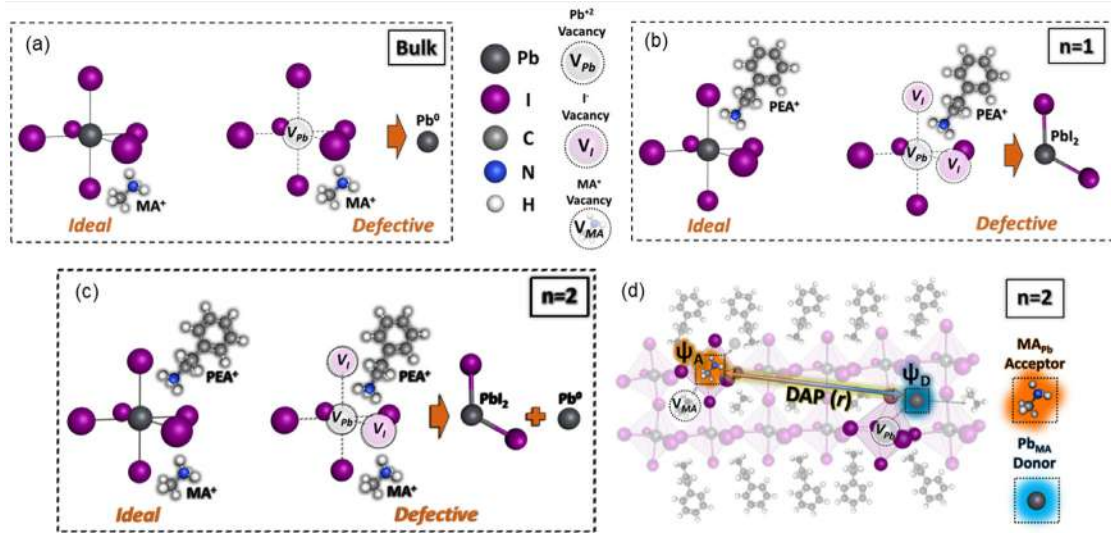


FIG. 6. Simplified scheme of ideal and defective PbI_6 octahedra units surrounded by different compositions of organic cations for each crystal phase with corresponding defects identified by XPS. Results indicate that (a) MA^+ cations present in bulk crystals seem to promote metallic Pb^0 segregation generating Pb vacancies (V_{Pb}), whereas (b) PEA_2^+ cations in $n = 1$ crystal phase tend to decompose inorganic sheets into lead iodine PbI_2 -like species favoring the generation of V_{Pb} and I vacancies (I_{Pb}). (c) Coexistence of both MA^+ and PEA_2^+ cations in $n = 2$ crystal phases enhances multiple defect generations. (d) The joint action of both MA^+ and PEA_2^+ cations in $n = 2$ crystals promotes the generation of MA_{Pb} acceptors, besides of Pb_{MA} donors. As a consequence, these two kinds of defects tend to form DAPs with a recombination emission energy that depends on their distance r .

that different organic components give rise to defects of different chemical nature: MA^+ cations somehow promote segregation of metallic Pb^0 , whereas PEA_2 cations tend to favor decomposition of inorganic sheets to produce PbI_2 -like species at the LHP surface.

The N 1s core-level XPS spectra are shown in Fig. 5(c). These data support the scenario proposed above. In our samples, the N 1s signal stems from the organic components of the 2D perovskites. In fact, in the bulk and in the 2D perovskite with $n = 1$, the dominant N 1s singlet signal comes from the MA^+ and PEA_2 cations, respectively [see upper and lower panels in Fig. 5(c)]. Only an additional weak signal can be observed at the low energy side of the N 1s spectrum measured in the bulk sample, which may be attributed to MA^+ cations in Pb sites (hereafter called the MA^+ defective). Indeed, the N 1s spectrum acquired in the 2D perovskite with $n = 2$ exhibits peaks coming from both the MA^+ and PEA_2 cations located at their own crystal sites [middle panel in Fig. 5(c)]. However, interestingly, a third important line is observed at lower energies than previous ones and clearly dominating. We identify this third state with the aforementioned MA^+ defective level, which now is shifted to lower binding energies than in the bulk perovskite, indicating that PEA_2 promotes the exchange of MA^+ cations with Pb in octahedral sites favoring MA^+ to act as acceptors. In summary, our XPS findings are compatible with the origin for the formation of DAP states from Pb_{MA} and MA_{Pb} antisite defects present in the RP $n = 2$ perovskites.⁴³

Perovskites can naturally host a wide variety of optically active defects whose optical recombination energy depends on their chemical nature.¹⁴ For instance, several defects acting as acceptors (I_i , MA_{Pb} , V_{MA} , V_{Pb} , I_{MA} , and I_{Pb}) or donors (MA_i , Pb_{MA} , V_i , Pb_i , MA_B , and Pb_B) have been found in 3D^{44–46} and 2D⁴³ LHPs (here, $V =$ vacancy, subscript $i =$ interstitial, and A_B denotes A substitutes for B).⁴⁵ Taking this into account, our XPS results reveal a rich n -dependent chemical

activity in 2D perovskites, which would give rise to optically active defects whose nature would depend on the specific organic component involved in and its dependence with the n value [see Figs. 6(a)–6(c)]. This fact becomes particularly relevant for disentangling optical properties of 2D perovskites with $n = 2$, in which both PEA_2 and MA^+ organic cations coexist in a similar proportion [see Fig. 1(c) or Fig. 6(c)]. Here, our hypothesis is that the joint action of the two organic cations present in the $n = 2$ perovskites is responsible for the generation of DAP complexes, as it is depicted in Fig. 6(d). MA^+ cations seem to promote Pb segregation, but the presence of PEA_2 cations, which strongly disturb the inorganic sheet, collaterally enhances the Pb segregation and favoring MA^+ cations to occupy Pb atomic sites within the perovskite octahedrals and creating the MA_{Pb} acceptors.⁴³ At the same time, displaced Pb atoms may occupy MA^+ sites out of the octahedrals, eventually acting as Pb_{MA} donors. It seems reasonable to assume that the effects of both cations were particularly efficient when acting on the same sites of the crystals; then, it would be expected that MA_{Pb} -related acceptors and Pb_{MA} -related donors are close to each other. Consequently, their wavefunctions would easily interact giving rise to DAPs complexes [Fig. 6(d)] and their observed spectral signatures in $\mu - PL$ experiments.

DISCUSSION

With the intention of evaluating our starting hypothesis of addressing the sharp $\mu - PL$ and long-lived $\mu - TRPL$ features found in the $n = 2$ phase with the DAP state optical recombination, suggested from the presented photoluminescence measurements, its sublinear intensity variation and saturation, and most directly by XPS and μ -Raman spectroscopy techniques, we test now our optical results with a simple model. Particularly, we will calculate the DOS of the

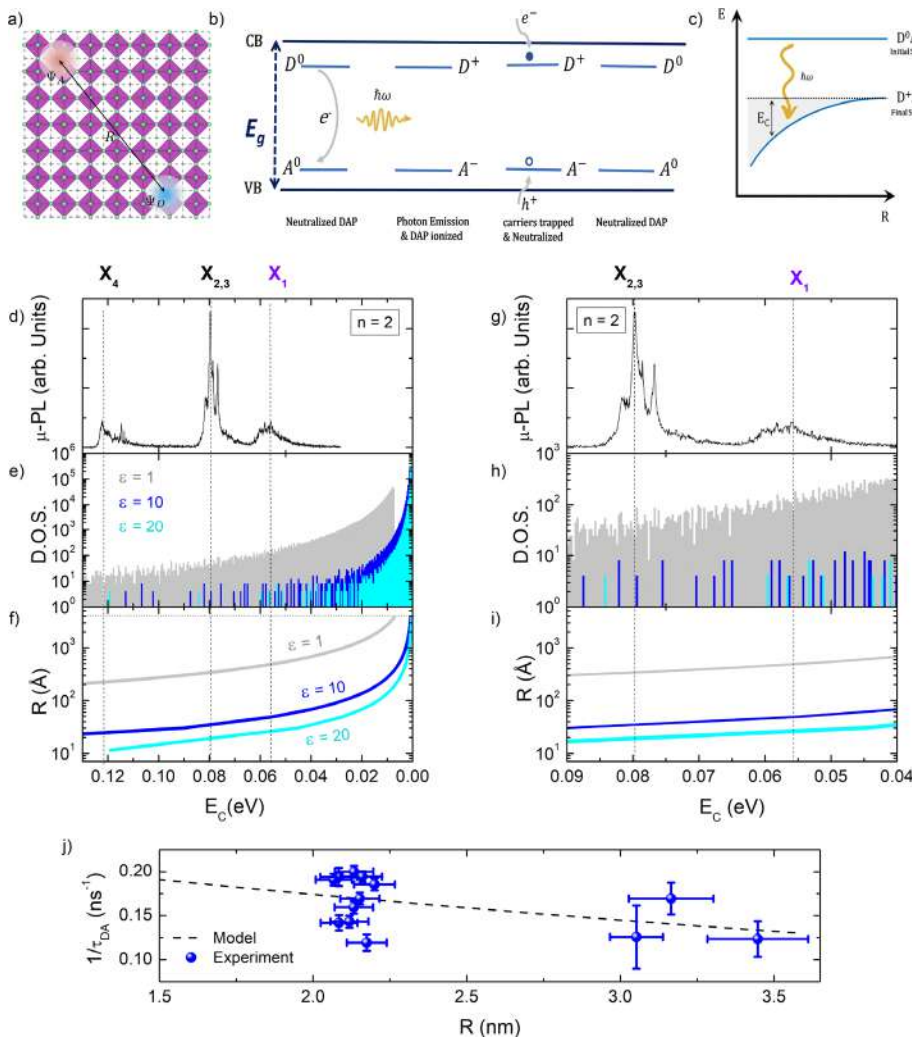


FIG. 7. (a) Sketch of the D^+A^- bonded complex state in a 2D perovskite lattice. R is the relative distance between D^+ and A^- wave functions. (b) DAP dynamical evolution: (from left to right) DAP ionization by the emission of a photon from the neutral D^0A^0 pair transition ($D^0A^0 = D^+A^- + \hbar\omega$), DAP neutralization from electron and hole capture processes ($D^+A^- + e^-_{CB} + h^+_{VB} = D^0A^0$). (c) D^0A^0 and D^+A^- level energies as a function of R . Grayish shadow indicates the magnitude of the D^+A^- binding energy (E_C) as a function of R . The emitted photon energy (wavy yellowish arrow) decreases as the distance R . (d) μ -Photoluminescence spectrum example plotting the four excitonic optical transitions present in $n=2$ samples. (e) Calculated DOS as a function of DAP binding energy (E_C) for three different Coulomb screenings ($\epsilon_r = 1, 10, \text{ and } 20$). (f) Calculated R value as a function of DAP binding energy (E_C) for three different Coulomb screenings ($\epsilon_r = 1, 10, \text{ and } 20$). (g)–(i) are zooms of plots (d)–(f), comprising the energy range between X_1 and $X_{2,3}$ optical transitions. (j) Inverse of the measured DAP decay time [τ_2 from Fig. 3(i)] as a function of the calculated R for $\epsilon_r = 10$. Black dashed line represents the best fit of the model described in the text.

DAP transitions and evaluate its decay time as a function of its binding energy and extract information about the DAP wavefunction.

Our model takes into account the presence of neutral donor (D^0) and neutral acceptor (A^0) levels, both defined with their corresponding binding energies. The spatial coordinate of their wave functions in the crystal structure will be separated with a relative distance R , as it is shown in Fig. 7(a). Figure 7(b) explains the dynamical process of the emission of a photon by the DAP complex. First, D^0 and A^0 do not form a bonded complex, as both do not have net charge. Second, each defect get ionized by the emission of a photon, i.e., the extra electron from D^0 relaxes to the extra hole state in A^0 , emitting a photon and producing the ionized D^+A^- pair. This ionized pair state, as we will explain later, is sensitive to the Coulomb's attraction between both positive and negative net charges. D^+ and A^- states can then be neutralized again by the capture of an electron (e^-) and a hole (h^+) from conduction band (CB) and valence band (VB), respectively. Finally, the neutral pair D^0A^0 can restart the photon emission cycle. Hence, this dynamical process is described with three main elementary processes: the (formation of the) initial state (D^0A^0), the emission of a

photon ($\hbar\omega$) followed by the (formation of the) final state (D^+A^-). Coulombic interaction (E_C) between D^+A^- obeys a relation inversely proportional to the distance between them (i.e., $E_C \propto \frac{1}{R}$). This means that the energy of the final state (D^+A^-) will change as a function of the relative distance R between the ionized donor D^+ and the ionized acceptor A^- . Figure 7(c) shows a visual scheme where the dependence with R is represented for the initial state D^0A^0 (no dependence), for the energy of the photon (smaller photon energy as R increases) and for the final state D^+A^- (smaller E_C as R increases). This physical picture allows us to model the DAP transition and to compare the output calculations with our μ -PL and μ -TRPL measurements. Following this procedure, we will estimate the possibility to find sharp-peaked transitions along the energy range between X_1 and $X_{2,3}$, extract the estimation of the D^+ and A^- binding energies, and hence their relative distances (R) and the corresponding donor and acceptor effective Bohr radius (a_D and a_A).

To develop our model, we assume the existence of D^0 and A^0 defect states within the bandgap, which here we associate their origin with the Pb_{Ma} (D) and Ma_{Pb} (A) antisite defects, as elucidated from

our previous XPS analysis. According to Ref. 43, density-functional theory calculation on two-dimensional $(\text{CH}_3\text{NH}_3)_2\text{Pb}(\text{SCN})_2\text{I}_2$ perovskites returns $\text{Pb}_{\text{Ma}}/\text{Ma}_{\text{Pb}}$ antisite defect transition at $\simeq 0.11$ eV/ $\simeq 0.15$ eV below the conduction band (CB)/above the valence band (VB). The energy of the emitted photon in a DAP transition defined by its relative distance R is given by

$$\hbar\omega(R) = E_{\text{GAP}} - E_A - E_D + \frac{e^2}{4\pi\epsilon_0\epsilon_r R}. \quad (1)$$

The term $E_C = \frac{e^2}{4\pi\epsilon_0\epsilon_r R}$ (DAP binding energy) accounts for the energy correction due to the Coulomb interaction between the ionized D^+A^- final state, which produces the corresponding change in the photon energy ($\hbar\omega$), as it is described above. Figure 7(a) shows the geometry of the square lattice of the 2D perovskites with a sketch of the D^+A^- bound final state. For the model calculations, we have assumed two inorganic layers 2D perovskite, to emulate the case with phase $n=2$. The DOS is obtained by calculating $\hbar\omega(R)$ for all possible R's between an electron in the donor site and the hole in the acceptor site. Here, it is important to mention that the calculation is done for a finite collection spot, obtained from the diffraction limit condition for the corresponding wavelength. This spot size will produce a limit for the maximum value of R, as we will define later. Figure 7(d) shows an example of the μ -PL spectrum of a $n=2$ sample, where the horizontal axis shows energy expressed in units of E_C . As a reference, it is included the energy positions of the four excitonic transitions found in the spectra [see Fig. 1(f)], with three vertical dashed lines fixed at $X_1, X_{2,3}$, and X_4 . Figure 7(e) shows the calculated DOS for three different values of the dielectric screening ($\epsilon = 1, 10$, and 20). The first situation, $\epsilon_r = 1$, represents the unscreened situation, which is typical of molecules or pure 2D monolayers. DOS as a function of E_C is represented with a grayish shadow. Clearly, the DOS is very large and dense through the whole energy range covering all four excitonic transitions. Therefore, it is not possible to find single DAP transitions within the evaluated spectral range if the effective dielectric screening was absent. This conclusion is reasonable, as these 2D RP perovskites contain long organic ligands, which clearly should increase the dielectric screening of the excitons photogenerated in the inorganic layers, as expected and found in the literature.²¹ Figure 7(f) shows the extracted R value from the model calculations as a function of E_C , for the same three values of the screening. Figure 7(c) clearly shows the E_C dependence on the calculated R value. When $R \rightarrow \infty$, $E_C = 0$, which corresponds to the extreme case for large R values represented in Fig. 7(c), where D^+A^- are largely separated and the Coulombic term becomes null. However, Fig. 7(f) shows a maximum and finite value for R [$\simeq 400$ nm, a limit plotted as a horizontal black dotted line in Fig. 7(f)] for all screening values, which corresponds with $R =$ collection spot size. This is the reason why the DOS in Fig. 7(e) suddenly drops for the corresponding E_B value associated with this value of R. Here, we have used the confocal diffraction limit as our collection spot size limit. When comparing R vs E_C dependence for the three different values of the screening, it is clearly shown that for a fixed value of E_C , when the dielectric constant increases, then the value of R decreases. In this way, to obtain equal binding energies using higher dielectric constants, the radius R should be smaller. In order to plot with higher resolution the DOS and R values as a function of E_C located in the vicinity of photon energies between X_1 and $X_{2,3}$ excitonic transitions, Figs. 7(g)–7(i) show zooms of the same data represented in Figs. 7(d)–7(f). Figures 7(e) and 7(h)

show that the use of $\epsilon_r = 10$ produces discrete states through the photon energy range of interest, along with a collapse of the DOS in the energy region near $E_C = 0$. If we further increase the value of the dielectric constant up to $\epsilon_r = 20$, it is clearly shown that the DOS collapse occurs in a narrower energy region around close to $E_C = 0$, hence with almost negligible occurrence of discrete states between X_1 and $X_{2,3}$ transitions.

A value of $\epsilon_r = 10.75$ between the static and the infinite frequency limit has been reported for single crystal of methylammonium lead bromide perovskite.²¹ Therefore, our model prediction for $\epsilon_r \simeq 10$ would be representative of a DOS closer to the real case and it will yield discrete DAP states between X_1 and $X_{2,3}$ excitonic transitions. Hence, $\epsilon_r \simeq 10$ is a good approximation for the actual dielectric screening. It is important to note here that although the $n = 1, 2, 3, \dots$, RP phases are defined by generating a quantum well-like confinement in the inorganic layer, the exfoliated samples are usually composed of multiple stackings of layers, forming samples of hundreds of nanometers of thickness.¹⁶ In the case of phase $n=1$, the stacking contains only this single phase, while in the case of $n > 1$, there may be heterogeneous mixtures of different RP n phases.

Once we have obtained a valid range of ϵ_r value, we can proceed to analyze the relation between DAP decay times and DAP binding energy (E_C), and hence to extract an estimation of the donor and acceptor Bohr radius. We use the following expression to extract the wavefunction extension dependence from the DAP decay time:^{47,48}

$$\frac{1}{\tau_{DA}} = \frac{\alpha}{\tau_X} \exp^{-2(R/a_{D,A})}, \quad (2)$$

where τ_{DA} and τ_X are the DAP and the excitonic decay times, R is the distance between D^+ and D^- extracted from the DAP binding energy values (E_C), $a_{D,A}$ are donor and acceptor Bohr radius, and α represents a constant of proportionality to be defined in the fit. This expression is reflecting an increase in τ_{DA} by increasing the DAP radius, because the smaller overlap between electron and hole overlap. Here, we use the mean τ_1 value of $X_{2,3}$ as τ_X [$\simeq 0.35$ ns, Fig. 2(j)]. We define τ_{DA} as a function of R from τ_2 values plotted in Fig. 3(i). The associated R values will be extracted using the expression of E_C and $\epsilon_r = 10$, as defined above. Finally, as the donor Bohr radius is usually larger in the tetrahedrally bonded semiconductors, then here we assume that $a_D > a_A$,⁴⁸ and therefore, we are basically extracting the value of a_D . Following all previous considerations in Fig. 7(j), it is shown the best fit of the expression 2 to the experimental data. The fit returns $\alpha = 0.09$ and $a_D \simeq 11$ nm. The value of a_D found in our fitting is around one order of magnitude larger than the excitonic Bohr radius calculated previously for 2D hybrid perovskites with $\epsilon_r = 10$.⁴⁹ This ratio is in correspondence with the fitted value of α , as this constant estimates the proportionality between τ_{DAP} and τ_X for $R = 0$. This large Bohr radius of the donor/acceptor wavefunction represents an important finding. Our study reveals that this large a_D is directly related to the extremely sharp spectral features ($\simeq 120$ μeV) and long-lived bonded DAP complexes.

CONCLUSIONS

In conclusion, our work shows that the research on DAP in 2D materials represents a growing field with high potential. Our observation of the narrow and discrete PL lines associated with discrete DAP transitions in 2D perovskites is added to recent reported properties

found in single-crystal perovskites.^{21–23} By means of XPS spectroscopy, we show that the two organic components present in the $n = 2$ sample promote the formation of the defects responsible of the DAP transition. In detail, the coexistence of MA^+ cation, giving rise to Pb segregation, and PEA_2 cation, causing the inorganic lattice sheet distortion, might favor the displacement and exchange of MA^+ and Pb atoms, hence the formation of MA_{Pb} acceptor and Pb_{MA} donor states. Our model predicts the presence of low-density DAP states in the spectral range close to the $X_{2,3}$ emission, and hence, both low DOS and large donor Bohr radius explain the observation of DAP narrow optical transitions with nanosecond lifetimes. The control of this large wavefunction extension photon emission process can be very attractive for future non-linear applications based on the control of the wavefunction overlap and spatial tunability. Nowadays, the use of highly bonded excitons but with larger wavefunction extensions represent desired route to build robust but highly interactive carriers, important to realize short- and long-range optically controllable interactions. These properties, together with its high photoluminescence brightness, make the DAP state in 2D perovskites an interesting electronic state to be considered in recent advanced quantum application proposals.^{29,50} However, in order for the DAP state present in these samples could be considered as an alternative, specific sample preparation routes should be designed to control and optimize the DAP state population, localization, and isolation.

EXPERIMENTAL

Synthesis

Materials were prepared by modifying a synthetic procedure that has been reported elsewhere.¹⁰ Synthesis of PEA_2PbI_4 ($n = 1$). Solution A. PbO powder (1116 mg, 5 mmol) was dissolved in a mixture of 57% w/w aqueous HI solution (5.0 ml, 38 mmol) and 50% aqueous H_3PO_2 (0.85 ml, 7.75 mmol) by heating to boiling under vigorous stirring for about 10 min. It was then possible to see the formation of a bright yellow solution. Solution B. In a separate beaker, $C_6H_5CH_2CH_2NH_2$ (phenethylamine, PEA) (628 μ l, 5 mmol) was neutralized with HI 57% w/w (2.5 ml, 19 mmol) in an ice bath, resulting in a clear pale-yellow solution. If a solid precipitate or the formation of a suspension is observed, then it is possible to heat slightly until it has dissolved. Once both solutions have been prepared, we proceed to the slow addition of Solution B to Solution A. A quick addition could produce a precipitate, which was subsequently dissolved as the combined solution was heated to boiling. After keep the solution at boiling point for 10 min, the stirring was then discontinued and the solution was left to cool to room temperature, during which time orange rectangular-shaped plates started to crystallize. The crystallization was deemed to be complete after 1 h. The crystals were isolated by suction filtration and thoroughly dried under reduced pressure. The obtained single crystals were washed with cold diethyl ether.

Synthesis of $PEA_2MAPb_2I_7$ ($n = 2$). Solution A. PbO powder (1116 mg, 5 mmol) was dissolved in a mixture of 57% w/w aqueous HI solution (5.0 ml, 38 mmol) and 50% aqueous H_3PO_2 (0.85 ml, 7.75 mmol) by heating to boiling under vigorous stirring for about 5 min and forming a yellow solution. Then, CH_3NH_3Cl powder (169 mg, 2.5 mmol) was added very slowly to the hot yellow solution, causing a black precipitate to form, which rapidly redissolved under stirring to achieve a clear bright yellow solution. Solution B. In a separate beaker, $C_6H_5CH_2CH_2NH_2$ (PEA) (880 μ l, 7 mmol) was

neutralized with HI 57% w/w w/w (2.5 ml, 19 mmol) in an ice bath, resulting in a clear pale-yellow solution. The addition of the PEA solution to the PbI_2 solution initially produces a black precipitate, which was dissolved under heating the combined solution to boiling. After discontinuing the stirring, the solution was cooled to room temperature, and cherry red crystals started to emerge. The precipitation was deemed to be complete after ~ 1 h. The crystals were isolated by suction filtration and thoroughly dried under reduced pressure. The material was washed with cold diethyl ether.

Crystal cleaving and sample preparation

A large statistical set of 2D PVKs and 3D single crystals was investigated. All of the measurements are carried out at room temperature. 2D PVKs crystals (PEA_2PbI_4 and $PEA_2MAPb_4I_7$) have been mechanically exfoliated on Si substrates by scotch tape.

Optical spectroscopy and confocal optical microscopy

All low-temperature measurements were carried out using a standard μ -PL setup, with the samples placed in the cold finger of a vibration-free closed-cycle cryostat (AttoDRY800 from Attocube AG). A continuous-wave (pulsed) excitation laser with a wavelength of $\lambda = 405$ nm (450 nm) was used to excite the sample, providing spectral μ -TRPL measurements. Furthermore, single-mode fiber-coupled laser diodes at $\lambda = 532$ and 660 nm were used to align the collection and excitation spots for 2D perovskite ($n = 1$, $n = 2$), respectively. The confocal pinholes will be defined by the single-mode optical fibers used for excitation and detection. Excitation and detection were carried out using a 50 \times microscope objective with a long working distance and a numerical aperture of $NA = 0.42$, which was placed outside the cryostat. The sample's emission was long-pass filtered, dispersed by a double 0.3 m focal length grating spectrograph (Acton SP-300i from Princeton Instruments), and detected with a cooled Si CCD camera (Newton EMCCD from ANDOR) for recording μ -PL spectra, and a silicon single-photon avalanche photodiode detector (from Micro Photon Devices) connected to a time-correlated single-photon counting electronic board (TCC900 from Edinburgh Instruments) for μ -TRPL measurements.⁵¹

Micro-Raman spectroscopy

Micro-Raman spectroscopy using a confocal Raman microscope Horiba-MTB Xplora was carried out using a red laser illumination with 638 nm excitation wavelength, 0.8–8 mW laser power, and 100 \times objective ($NA = 0.9$, $WD = 0.21$ mm).

X-ray photoelectron spectroscopy

Part of the x-ray photoemission experiments was performed at the ALOISA beamline of the Elettra Sincrotrone of Trieste, Italy.⁵² In this case, the x-ray photon energy of 515 eV (overall resolution of 150 meV, FWHM) was used for C 1s, N 1s, and Pb 4f core levels and photon energy of 740 eV (overall resolution of 280 meV) was used for I 3d core levels. The samples ($n = 1$ and 2) were kept at a grazing angle of 4 $^\circ$ in close to p-polarization. The spectra were measured in normal emission with a homemade hemispherical spectrometer (mean radius of 66 mm) equipped with the Elettra 2D delay-line detector. The other part of the XPS experiments was performed in a SPECS GmbH system

(base pressure 1.0×10^{-10} mbar) equipped with a ASTRAIOS 190 2D-CMOS hemispherical analyzer. Energy resolution was found in the range of 0.1 eV. Photoelectrons were excited with the Al-K α line (1486.7 eV) of a monochromatic x-ray source μ -FOCUS 500 (SPECS GmbH). In the high resolution (HR)-XPS experiments performed, the spot size was about 0.5 mm in diameter. Measurements were taken at room temperature with a pass-energy of 20 eV. For all of the HR-XPS measurements, freshly exfoliated 2D PVKs were exposed to air and placed in ultrahigh vacuum (UHV) conditions (with an analysis chamber base pressure lower than 1.0×10^{-10} mbar). In contrast, 3D samples were just grown and immediately introduced into the UHV chamber to avoid any perturbation of the surface species induced from being in contact with standard atmospheric conditions.

ACKNOWLEDGMENTS

This study forms part of the Advanced Materials program and was supported by MCIN with funding from European Union NextGenerationEU (PRTR-C17.I1) and by Generalitat Valenciana, with Ref. 20220883 (PerovsQuTe), the Horizon 2020 research and innovation program of the EU through the S2QUIP project (Grant Agreement No. 8204023), the Ministerio de Ciencia e Innovación, which is part of Agencia Estatal de Investigación (AEI), through the Project PID2020-112507GB-I00 (Novel quantum states in heterostructures of 2D materials), PID2020-120484RB-I00 (PERIPHERAL), and PID2019-107314RB-I00 (Stable), and the Generalitat Valenciana through the Grant No. PROMETEO 2021/082 (ENIGMA), Grant No. SEJIGENT 2021/034 (2D-MAGNONICS), and Grant No. MFA 2022/009 (SPINO2D). This study forms part of the Advanced Materials programme and was supported by MCIN with funding from European Union NextGenerationEU (PRTR-C17.I1) and by Generalitat Valenciana. The research leading to this result has been supported by the project CALIPSOplus under Grant Agreement No. 730872 from the EU Framework Programme for Research and Innovation HORIZON 2020. A.M. acknowledges the Ramón y Cajal programme (Grant RYC2018-024024-I; MINECO, Spain). M.K. acknowledges the APOSTD programme (Contract No. APOSTD/2020/103), and G.M. thanks the Ramón y Cajal programme (Contract No. RYC2020-030099-I).

AUTHOR DECLARATIONS

Conflict of Interest

The authors have no conflicts to disclose.

Author Contributions

Setatira Gorji and Marie Krečmarová contributed equally to this paper.

Setatira Gorji: Data curation (equal); Investigation (equal); Writing – original draft (supporting); Writing – review & editing (supporting). **Marie Krečmarová:** Data curation (equal); Investigation (equal); Writing – original draft (supporting); Writing – review & editing (supporting). **Alejandro Molina:** Formal analysis (equal); Investigation (supporting); Methodology (supporting); Resources (supporting); Software (lead); Writing – original draft (supporting); Writing – review & editing (supporting). **María C. Asensio:** Formal analysis (equal); Investigation

(supporting); Methodology (supporting); Writing – review & editing (supporting). **Andres F. Gualdron-Reyes:** Investigation (supporting). **Jesus Rodriguez-Romero:** Investigation (supporting). **Hamid Pashaei Adl:** Investigation (supporting). **Rodolfo Canet-Albiach:** Investigation (equal). **Luca Schio:** Investigation (supporting). **Massimo Tormen:** Investigation (supporting). **Luca Floreano:** Investigation (supporting). **Ivan Mora-Sero:** Conceptualization (supporting); Investigation (supporting); Methodology (supporting); Resources (supporting); Writing – review & editing (supporting). **Juan P. Martinez Pastor:** Conceptualization (supporting); Project administration (lead); Resources (lead); Supervision (equal); Validation (supporting); Writing – review & editing (equal). **J. F. Sanchez-Royo:** Investigation (supporting); Methodology (supporting); Resources (supporting). **Guillermo Muñoz-Matutano:** Conceptualization (lead); Data curation (equal); Formal analysis (lead); Investigation (lead); Methodology (lead); Project administration (lead); Supervision (equal); Visualization (equal); Writing – original draft (equal); Writing – review & editing (lead).

DATA AVAILABILITY

The data that support the findings of this study are available from the corresponding author upon reasonable request.

REFERENCES

- 1A. Vinattieri and G. Giorgi, “Halide perovskites for photonics: Recent history and perspectives,” in *Halide Perovskites for Photonics* (AIP Publishing, 2021).
- 2A. Kojima, K. Teshima, Y. Shirai, and T. Miyasaka, “Organometal halide perovskites as visible-light sensitizers for photovoltaic cells,” *J. Am. Chem. Soc.* **131**, 6050–6051 (2009).
- 3J.-C. Blancon, J. Even, C. C. Stoumpos, M. G. Kanatzidis, and A. D. Mohite, “Semiconductor physics of organic-inorganic 2D halide perovskites,” *Nat. Nanotechnol.* **15**, 969–985 (2020).
- 4P. Zhu and J. Zhu, “Low-dimensional metal halide perovskites and related optoelectronic applications,” *InfoMat* **2**, 341–378 (2020).
- 5D. H. Cao, C. C. Stoumpos, O. K. Farha, J. T. Hupp, and M. G. Kanatzidis, “2D homologous perovskites as light-absorbing materials for solar cell applications,” *J. Am. Chem. Soc.* **137**, 7843–7850 (2015).
- 6L. Dou, “Emerging two-dimensional halide perovskite nanomaterials,” *J. Mater. Chem. C* **5**, 11165–11173 (2017).
- 7A. G. Ricciardulli, S. Yang, J. H. Smet, and M. Saliba, “Emerging perovskite monolayers,” *Nat. Mater.* **20**, 1325–1336 (2021).
- 8R. Krahn, “Two-dimensional layered perovskites for photonic devices,” in *Halide Perovskites for Photonics* (AIP Publishing, 2021).
- 9K. Leng, W. Fu, Y. Liu, M. Chhowalla, and K. P. Loh, “From bulk to molecularly thin hybrid perovskites,” *Nat. Rev. Mater.* **5**, 482–500 (2020).
- 10C. C. Stoumpos, D. H. Cao, D. J. Clark, J. Young, J. M. Rondinelli, J. I. Jang, J. T. Hupp, and M. G. Kanatzidis, “Ruddlesden–Popper hybrid lead iodide perovskite 2D homologous semiconductors,” *Chem. Mater.* **28**, 2852–2867 (2016).
- 11X. Xiao, J. Zhou, K. Song, J. Zhao, Y. Zhou, P. N. Rudd, Y. Han, J. Li, and J. Huang, “Layer number dependent ferroelasticity in 2D Ruddlesden–Popper organic-inorganic hybrid perovskites,” *Nat. Commun.* **12**, 1332 (2021).
- 12M. Seitz, A. J. Magdaleno, N. Alcázar-Cano, M. Meléndez, T. J. Lubbers, S. W. Walraven, S. Pakdel, E. Prada, R. Delgado-Buscalioni, and F. Prins, “Exciton diffusion in two-dimensional metal-halide perovskites,” *Nat. Commun.* **11**, 2035 (2020).
- 13L. Zhao, Y. L. Lin, H. Kim, N. C. Giebink, and B. P. Rand, “Donor/acceptor charge-transfer states at two-dimensional metal halide perovskite and organic semiconductor interfaces,” *ACS Energy Lett.* **3**, 2708–2712 (2018).
- 14Y. Lekina and Z. X. Shen, “Excitonic states and structural stability in two-dimensional hybrid organic-inorganic perovskites,” *J. Sci.: Adv. Mater. Devices* **4**, 189–200 (2019).
- 15T. T. H. Do, A. Granados del Aguila, D. Zhang, J. Xing, S. Liu, M. Prosnikov, W. Gao, K. Chang, P. C. Christianen, and Q. Xiong, “Bright exciton fine-

- structure in two-dimensional lead halide perovskites," *Nano Lett.* **20**, 5141–5148 (2020).
- ¹⁶R. Canet-Albiach, M. Krecmarova, J. B. Bailach, A. F. Gualdrón-Reyes, J. Rodríguez-Romero, S. Gorji, H. Pashaei-Adl, I. Mora-Seró, J. P. Martínez Pastor, and J. F. Sánchez-Royo, "Revealing giant exciton fine-structure splitting in two-dimensional perovskites using van der Waals passivation," *Nano Lett.* **22**, 7621–7627 (2022).
- ¹⁷M. A. Green, A. Ho-Baillie, and H. J. Snaith, "The emergence of perovskite solar cells," *Nat. Photonics* **8**, 506–514 (2014).
- ¹⁸R. Su, S. Ghosh, J. Wang, S. Liu, C. Diederichs, T. C. H. Liew, and Q. Xiong, "Observation of exciton polariton condensation in a perovskite lattice at room temperature," *Nat. Phys.* **16**, 301 (2020).
- ¹⁹M. Leng, J. Wu, K. Dini, J. Liu, Z. Hu, J. Tang, T. C. H. Liew, H. Sun, R. Su, and Q. Xiong, "Optically pumped polaritons in perovskite light-emitting diodes," *ACS Photonics* **10**, 1349 (2023).
- ²⁰J. V. Passarelli, C. M. Mauck, S. W. Winslow, C. F. Perkinson, J. C. Bard, H. Sai, K. W. Williams, A. Narayanan, D. J. Fairfield, and M. P. Hendricks, "Tunable exciton binding energy in 2D hybrid layered perovskites through donor–acceptor interactions within the organic layer," *Nat. Chem.* **12**, 672–682 (2020).
- ²¹J. Tilchin, D. N. Dirin, G. I. Maikov, A. Sashchiuk, M. V. Kovalenko, and E. Lifshitz, "Hydrogen-like Wannier-Mott excitons in single crystal of methylammonium lead bromide perovskite," *ACS Nano* **10**, 6363 (2016).
- ²²A. Francisco-López, B. Charles, M. I. Alonso, M. Garriga, M. T. Weller, and A. R. Goi, "Photoluminescence of bound-exciton complexes and assignment to shallow defects in methylammonium/formamidinium lead iodide mixed crystals," *Adv. Opt. Mater.* **9**, 2001969 (2021).
- ²³J. M. Urban, T. H. T. Nguyen, G. Chehade, A. Delteil, G. Trippé-Allard, G. Delpont, E. Deleporte, J.-P. Hermier, and D. Garrot, "Discrete donor-acceptor pair transitions in CH₃NH₃PbI₃ perovskite single crystals," *Phys. Status Solidi RRL* **17**, 2300005 (2023).
- ²⁴Q. Tan, J.-M. Lai, X.-L. Liu, D. Guo, Y. Xue, X. Dou, B.-Q. Sun, H.-X. Deng, P.-H. Tan, and I. Aharonovich, "Donor–acceptor pair quantum emitters in hexagonal boron nitride," *Nano Lett.* **22**, 1331–1337 (2021).
- ²⁵S. Kahmann, E. K. Tekelenburg, H. Duim, M. E. Kamminga, and M. A. Loi, "Extrinsic nature of the broad photoluminescence in lead iodide-based Ruddlesden–Popper perovskites," *Nat. Commun.* **11**, 2344 (2020).
- ²⁶R. Su, A. Fieramosca, Q. Zhang, H. S. Nguyen, E. Deleporte, Z. Chen, D. Sanvitto, T. C. Liew, and Q. Xiong, "Perovskite semiconductors for room-temperature exciton-polaritonics," *Nat. Mater.* **20**, 1315–1324 (2021).
- ²⁷G. Muñoz-Matutano, A. Wood, M. Johansson, X. Vidal, B. Q. Baragiola, A. Reinhard, A. Lemaître, J. Bloch, A. Amo, and G. Nogues, "Emergence of quantum correlations from interacting fibre-cavity polaritons," *Nat. Mater.* **18**, 213–218 (2019).
- ²⁸A. Delteil, T. Fink, A. Schade, S. Höfling, C. Schneider, and A. İmamoglu, "Towards polariton blockade of confined exciton–polaritons," *Nat. Mater.* **18**, 219–222 (2019).
- ²⁹A. Bilgin, I. N. Hammock, J. Estes, Y. Jin, H. Bernien, A. A. High, and G. Galli, "Donor-acceptor pairs in wide-bandgap semiconductors for quantum technology applications," *npj Comput. Mater.* **10**, 7 (2024).
- ³⁰Y. Chen, Y. Sun, J. Peng, J. Tang, K. Zheng, and Z. Liang, "2D Ruddlesden–Popper perovskites for optoelectronics," *Adv. Mater.* **30**, 1703487 (2018).
- ³¹J. Li, J. Wang, Y. Zhang, H. Wang, G. Lin, X. Xiong, W. Zhou, H. Luo, and D. Li, "Fabrication of single phase 2D homologous perovskite microplates by mechanical exfoliation," *2D Mater.* **5**, 021001 (2018).
- ³²B. Dhanabalan, A. Castelli, M. Palei, D. Spirito, L. Manna, R. Krahne, and M. Arciniegas, "Simple fabrication of layered halide perovskite platelets and enhanced photoluminescence from mechanically exfoliated flakes," *Nanoscale* **11**, 8334–8342 (2019).
- ³³P. C. Sercel, J. L. Lyons, D. Wickramaratne, R. Vaxenburg, N. Bernstein, and A. L. Efros, "Exciton fine structure in perovskite nanocrystals," *Nano Lett.* **19**, 4068 (2019).
- ³⁴W. Li, C. Fang, H. Wang, S. Wang, J. Li, J. Ma, J. Wang, H. Luo, and D. Li, "Surface depletion field in 2D perovskite microplates: Structural phase transition, quantum confinement and Stark effect," *Nano Res.* **12**, 2858–2865 (2019).
- ³⁵C. Mi, M. L. Atteberry, V. Mapara, L. Hidayatova, G. C. Gee, M. Furis, W. T. Yip, B. Weng, and Y. Dong, "Biexciton-like auger blinking in strongly confined CsPbBr₃ perovskite quantum dots," *J. Phys. Chem. Lett.* **14**, 5466–5474 (2023).
- ³⁶V. S. Chirvony, S. González-Carrero, I. Suárez, R. E. Galian, M. Sessolo, H. J. Bolink, J. P. Martínez-Pastor, and J. Pérez-Prieto, "Delayed luminescence in lead halide perovskite nanocrystals," *J. Phys. Chem. C* **121**, 13381 (2017).
- ³⁷Y. Yang, Y. Yan, M. Yang, S. Choi, K. Zhu, J. M. Luther, and M. C. Beard, "Low surface recombination velocity in solution-grown CH₃NH₃PbBr₃ perovskite single crystal," *Nat. Commun.* **6**, 7961 (2015).
- ³⁸T. Schmidt, K. Lischka, and W. Zulehner, "Excitation-power dependence of the near-band-edge photoluminescence of semiconductors," *Phys. Rev. B* **45**, 8989 (1992).
- ³⁹N. Aihara, K. Tanaka, H. Uchiki, A. Kanai, and H. Araki, "Donor-acceptor pair recombination luminescence from monoclinic Cu₂SnS₃ thin film," *Appl. Phys. Lett.* **107**, 032101 (2015).
- ⁴⁰A. Berthelot, I. Favero, G. Cassabois, C. Voisin, C. Delalande, P. Roussignol, R. Ferreira, and J.-M. Gérard, "Unconventional motional narrowing in the optical spectrum of a semiconductor quantum dot," *Nat. Phys.* **2**, 759–764 (2006).
- ⁴¹R. Dingle and M. Ilegems, "Donor-acceptor pair recombination in GaN," *Solid State Commun.* **9**, 175–180 (1971).
- ⁴²P. Pistor, A. Ruiz, A. Cabot, and V. Izquierdo-Roca, "Advanced Raman spectroscopy of methylammonium lead iodide: Development of a non-destructive characterisation methodology," *Sci. Rep.* **6**, 35973 (2016).
- ⁴³Z. Xiao, W. Meng, J. Wang, and Y. Yan, "Defect properties of the two-dimensional (CH₃NH₃)₂Pb(SCN)₂I₂ perovskite: A density-functional theory study," *Phys. Chem. Chem. Phys.* **18**, 25786–25790 (2016).
- ⁴⁴F. Wang, S. Bai, W. Tress, A. Hagfeldt, and F. Gao, "Defects engineering for high-performance perovskite solar cells," *npj Flexible Electron.* **2**, 22 (2018).
- ⁴⁵A. Merdasa, Y. Tian, R. Camacho, A. Dobrovolsky, E. Debroye, E. L. Unger, J. Hofkens, V. Sundstrom, and I. G. Scheblykin, "Supertrap" at work: Extremely efficient nonradiative recombination channels in MAPbI₃ perovskites revealed by luminescence super-resolution imaging and spectroscopy," *ACS Nano* **11**, 5391–5404 (2017).
- ⁴⁶W.-J. Yin, T. Shi, and Y. Yan, "Unusual defect physics in CH₃NH₃PbI₃ perovskite solar cell absorber," *Appl. Phys. Lett.* **104**, 063903 (2014).
- ⁴⁷W. Kong, Z. Ye, Z. Qi, B. Zhang, M. Wang, A. Rahimi-Imanc, and H. Wu, "Characterization of an abnormal photoluminescence behavior upon crystal-phase transition of perovskite CH₃NH₃PbI₃," *Phys. Chem. Chem. Phys.* **17**, 16405 (2015).
- ⁴⁸P. Y. Yu and M. Cardona, *Fundamentals of Semiconductors. Physics and Materials Properties* (Springer, Berlin, Heidelberg, 2010).
- ⁴⁹B. Cheng *et al.*, "Extremely reduced dielectric confinement in two-dimensional hybrid perovskites with large polar organics," *Commun. Phys.* **1**, 80 (2018).
- ⁵⁰P. Stepanov, A. Vashisht, M. Klaas, N. Lundt, S. Tongay, M. Blei, S. Höfling, T. Volz, A. Minguzzi, J. Renard, C. Schneider, and M. Richard, "Exciton-exciton interaction beyond the hydrogenic picture in a MoSe₂ monolayer in the strong light-matter coupling regime," *Phys. Rev. Lett.* **126**, 167401 (2021).
- ⁵¹H. P. Adl, S. Gorji, G. Muñoz-Matutano, R. I. Sánchez-Alarcón, R. Abargues, A. F. Gualdrón-Reyes, I. Mora-Seró, and J. P. Martínez-Pastor, "Homogeneous and inhomogeneous broadening in single perovskite nanocrystals investigated by micro-photoluminescence," *J. Lumin.* **240**, 118453 (2021).
- ⁵²L. Floreano, A. Cossaro, R. Gotter, A. Verdini, G. Bavdek, F. Evangelista, A. Ruocco, A. Morgante, and D. Cvetko, "Periodic arrays of Cu-phthalocyanine chains on Au(110)," *J. Phys. Chem. C* **112**, 10794–10802 (2008).